

## Competing Liquid Phase Instabilities during Pulsed Laser Induced Self-Assembly of Copper Rings into Ordered Nanoparticle Arrays on SiO<sub>2</sub>

Y. Wu,<sup>†</sup> J. D. Fowlkes,<sup>‡</sup> N. A. Roberts,<sup>‡</sup> J. A. Diez,<sup>§</sup> L. Kondic,<sup>||</sup> A. G. González,<sup>§</sup> and P. D. Rack\*,<sup>\*,†,‡</sup>

<sup>†</sup>Department of Materials Science and Engineering, The University of Tennessee, Knoxville, Tennessee 37996, United States

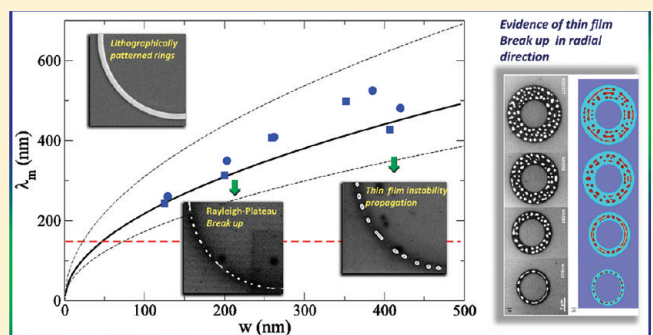
<sup>‡</sup>Nanofabrication Research Laboratory, Center for Nanophase Materials Sciences, Oak Ridge National Laboratory, Oak Ridge, Tennessee 37831, United States

<sup>§</sup>Instituto de Física Arroyo Seco, Universidad Nacional del Centro de la Provincia de Buenos Aires, Pinto 399, 7000 Tandil, Argentina

<sup>||</sup>Department of Mathematical Sciences, Center for Applied Mathematics and Statistics, New Jersey Institute of Technology, Newark, New Jersey 07102, United States

 Supporting Information

**ABSTRACT:** Nanoscale copper rings of different radii, thicknesses, and widths were synthesized on silicon dioxide thin films and were subsequently liquefied via a nanosecond pulse laser treatment. During the nanoscale liquid lifetimes, the rings experience competing retraction dynamics and thin film and/or Rayleigh–Plateau types of instabilities, which lead to arrays of ordered nanodroplets. Surprisingly, the results are significantly different from those of similar experiments carried out on a Si surface.<sup>1</sup> We use hydrodynamic simulations to elucidate how the different liquid/solid interactions control the different instability mechanisms in the present problem.



### 1. INTRODUCTION

The synthesis and assembly of functional nanoparticles via metallic thin film dewetting has the potential to be an effective way to realize nanoparticle ensembles for a variety of applications including sensors, information processing, photovoltaics, catalysis,<sup>2–4</sup> and plasmonics.<sup>5–11</sup> In recent years, many theoretical and experimental studies have focused on the instability and breakup of two-dimensional (2D) thin films particularly for thicknesses under ~50 nm, where gravity is negligible with respect to capillary and liquid–solid interaction forces and nanometer size particles can be formed.<sup>12–19</sup>

The instability mechanism which governs the breakup on the nanoscale is strongly influenced by the initial geometry of the film. Considering first thin films, the two generally accepted mechanisms that dominate are nucleation and the so-called spinodal instability. The nucleation case may be initiated by either thermal fluctuations or defects in the film or substrate and yields a spatially uncorrelated distribution of nanoparticles, while under a spinodal mechanism film breakup is a result of the amplification of infinitesimal surface perturbations. This latter mechanism leads to spatially ordered nanoparticles with a characteristic length scale determined approximately by the most unstable wavelength.<sup>13,19–21</sup> The initial nanoparticle length scale is often set by the spinodal wavelength; however, the coalescence of neighboring holes often

leads to rim formation and their subsequent breakup via a mechanism which resembles a Rayleigh–Plateau (R-P) instability.<sup>17</sup>

The instability and consequent breakup of thin rivulets have also been a subject of study relevant to applications in the field of nanofluidics.<sup>22–25</sup> At the nanoscale, a thin film and an R-P type of unstable behavior that takes into account the presence of contact lines can compete. In our previous work,<sup>1</sup> where we discussed breakup of Cu rings on a Si surface, we found that this competition may lead to a transition from one to another type of instability, with the mechanism characterized by the fastest time scale being dominant. We note that instabilities of liquid rivulets have been extensively studied in the past. Young and Davis<sup>26</sup> studied the rivulet on an inclined surface where an axial flow can be observed due to gravity. Brochard-Wyart and Redon<sup>21</sup> reported the study of rivulet stability based on analysis of the free energy, whereas Sekimoto et al.<sup>27</sup> studied spatial perturbations of the rivulet steady state solution by minimizing surface energy, and Langbein<sup>28</sup> explored the rivulet on a plane substrate by treating the problem as a particular case of flow in a wedge. On the particular relevance to the problem discussed in this paper is the work by González, Diez, and Kondic,

**Received:** August 12, 2011

**Revised:** September 14, 2011

**Published:** September 15, 2011

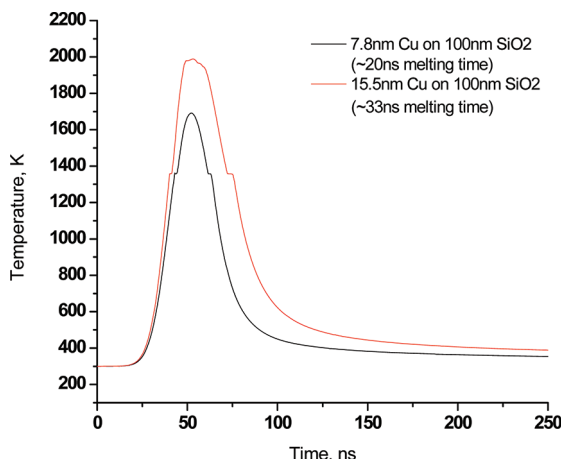


**Figure 1.** Time–temperature simulation of 7.8 nm Cu on 100 nm SiO<sub>2</sub> and 15 nm Cu on 100 nm SiO<sub>2</sub>.

where the dynamics of the contact line and its subsequent destabilization were studied using a van der Waals model.<sup>22</sup>

To complement the numerous investigations studying instability propagation and the self-assembly of subsequent nanoparticle arrays, we have recently investigated the directed assembly of pulsed laser treated nanolithographically patterned metal films. Specifically, we have investigated lithographically patterned lines,<sup>29</sup> triangles,<sup>30,31</sup> and more recently rings<sup>1</sup> and templated lines with so-called “synthetic perturbations”.<sup>32</sup> An interesting competition between thin film and R-P types of instabilities was recently observed for pulsed laser induced dewetting of nanolithographically patterned Cu rings of various sizes (diameter, width, and thickness) on silicon. Specifically, it was observed that when the cumulative transport and R-P time scale were shorter than the thin film instability time scale, the Cu nanoparticles are characterized by the distance consistent with the R-P instability. Conversely, when the thin film instability time scale was shorter than the cumulative retraction and R-P time scale, a 2D array was observed, consistent with the thin film instability. To follow up on the previous work, here we investigate experimentally the liquid phase breakup of nanoscale Cu rings lithographically patterned on a SiO<sub>2</sub> substrate, which has different energetics and thus transport and instability time scales. Furthermore, we carry out numerical simulation and theoretical analysis, and discuss the degree to which existing theory explains and predicts experimental results.

## 2. EXPERIMENT

Initially three identical sets of copper rings with two thicknesses ( $\sim$ 7.8 and 15 nm), two radii (5 and 10  $\mu\text{m}$ , sufficiently large for the Laplace pressure due to azimuthal curvature to be negligible), and variable ring widths (ranging from 103 to 420 nm) were patterned onto a (100)-oriented single crystal silicon wafer coated with a 100 nm SiO<sub>2</sub> film. Ring geometries were studied as they conveniently eliminate competing effects that occur at the end of finite lines and thus mimic an infinite line. A total of 60 rings was considered. The purpose of having three identical rings for each type was to confirm the repeatability of the instability length scale. The lithographically patterned ring widths were measured via scanning electron microscopy (SEM). Each ring was electron beam patterned into a positive tone thin

polymethylmethacrylate (PMMA) film. Copper films of 15 and 7.8 nm (as measured by atomic force microscopy) were subsequently sputter deposited, and the ring pattern was realized by dissolving or “lifting-off” of the original PMMA film in an acetone bath for  $\sim$ 1 h. Subsequently, a KrF 18 ns pulsed excimer laser at 248 nm wavelength was used to simultaneously irradiate all of the ring patterns (for each copper thickness) with five laser pulses at a fluence of 160 mJ/cm<sup>2</sup>, which is sufficient to melt the copper film and ultimately form an array of ordered nanodrops. The simulated melting time for each pulse is  $\sim$ 33 ns for the 15 nm thickness rings and  $\sim$ 22 ns for the 7.8 nm thickness rings estimated by a time–temperature simulation as plotted in Figure 1. Figures 2a and 3a are electron micrographs of 5  $\mu\text{m}$  radius rings with initial thicknesses of 7.8 and 15 nm, respectively, which demonstrate the resultant nanoparticle arrays after five laser pulses. The average particle spacings (number of particles divided by the circumference) of the 5 and 10  $\mu\text{m}$  radius rings as a function of the measured ring width for the 7.8 and 15 nm thickness rings are plotted in Figures 2b and 3b, respectively.

In addition to average particle spacing, it is of interest to consider the distribution of the spacing between drops in any given experiment. These distributions are important since, as we discuss in more detail later in the paper, they allow for more meaningful comparison of theoretical and computational results. As an example, the inset in Figure 2b shows a typical histogram of the nanoparticle spacing for a 7.8 nm thick and 407 nm wide ring (5  $\mu\text{m}$  radius), and the inset in Figure 3b gives a typical histogram of the nanoparticle spacing for a 15 nm thick and 380 nm wide ring (5  $\mu\text{m}$  radius). Due to the conservation of mass, the resultant dispersion in the nanoparticle spacing also results in a dispersion in the nanoparticle radii (not shown). Clearly, a dispersion of the experimental particle spacings needs to be considered when comparing to a theoretical model.

The mass loss of the copper ring during pulsed laser dewetting was calculated by summing the volume of the dewetted nanoparticles in a specific area. The individual nanoparticle volume ( $V$ ) was calculated from the expression  $V = \pi(R/\sin \theta)^3[2 - 3\cos \theta - \cos^3 \theta]$ , where  $\theta$  is the measured contact angle of 79° and  $R$  is the particle radius.<sup>19</sup> We compare the resulting nanoparticle volume to the original thin film volume (area times thickness). The mass loss was estimated to be <2% per pulse, which is much less than the mass loss observed on the Si substrate. We attribute this small loss to the lower diffusion rate of copper in SiO<sub>2</sub>.<sup>33</sup>

Figures 2 and 3 show the formation of ordered rings of nanoparticles whose spacings (and sizes) follow a smooth and monotonic increase with increased ring width, although the 7.8 nm case possibly shows some growth saturation for larger widths at approximately 350 nm ring width. Interestingly, these phenomena are clearly different from the previous results for 7 and 13 nm copper rings dewetted on a Si substrate as discussed recently,<sup>1</sup> where the 13 nm copper rings show an average spacing shifting to a lower constant value at  $\sim$ 215 nm ring width, and the 7 nm copper rings exhibit radial breakup for ring width above approximately 330 nm. One might expect that the monotonic increase of average spacing with ring width is consistent with the contraction of the rings to semicylindrical strips and the subsequent breakup due to a Rayleigh–Plateau type of instability, modified by the presence of SiO<sub>2</sub> substrate<sup>21,29,34,35</sup> (except perhaps for the 7.8 nm thickness rings with width  $>\sim$ 350 nm). The question remains: is this an accurate explanation

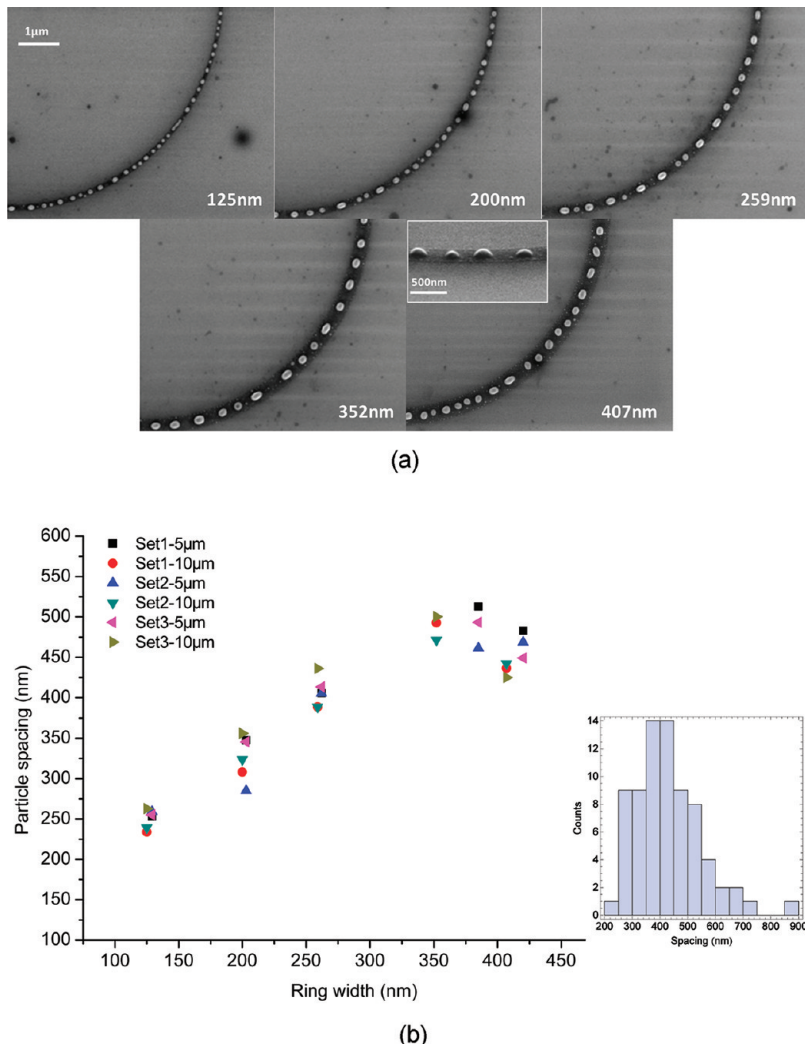


**Figure 2.** (a) Scanning electron micrographs of the  $h_0 = 7.8$  nm thick, 5  $\mu\text{m}$  radius copper rings of variable widths after 5 pulses. Inset: 60° tilted scanning electron micrographs of the  $h_0 = 7.8$  nm thick, 5  $\mu\text{m}$  radius copper rings of 407 nm width. (b) Plot of average nanodrop spacing for fifteen 5  $\mu\text{m}$  and fifteen 10  $\mu\text{m}$  radius rings as a function of the measured widths. Inset shows the histogram of the droplet spacing (lower right) for 407 nm wide rings of 5  $\mu\text{m}$  radius.

of ring breakup? Based on our previous work studying Cu on silicon substrates, can this phenomenon be explained by the competition of time scales relevant to different instability mechanisms? Can we predict and explain the liquid ring breakup using a simple hydrodynamic model? One important goal of this study is to answer these questions.

### 3. MODEL

We model both the transport and instability processes during the liquid lifetime by assuming that the liquid metal behaves like a Newtonian fluid (see also refs 1 and 29 regarding this point). We also assume that the pulsed laser irradiation leads to very rapid heating so that all thermal related effects take place on a time scale which is much faster than the time scale of the evolution. Thus, we assume the metal liquid at a fixed and uniform temperature.

The dynamics are described by using a long wave (lubrication) approximation which allows reducing the Navier–Stokes equation to a single differential equation for the fluid thickness.<sup>22,29</sup> This approach leads to the following nonlinear fourth order

partial differential equation,<sup>36</sup>

$$3\mu \frac{\partial h}{\partial t} + \gamma \nabla \cdot (h^3 \nabla \nabla^2 h) + \nabla \cdot [h^3 \nabla \prod(h)] = 0 \quad (1)$$

where  $h(x, y, t)$  is the film thickness,  $x$  and  $y$  are the in-plane coordinates,  $\nabla = (\partial/\partial x, \partial/\partial y)$ ,  $\mu$  is the dynamic viscosity, and  $\gamma$  is the surface tension. Here, the second term corresponds to the capillary forces, and the third term is due to the liquid–solid interaction. The functional form of the disjoining pressure,  $\prod(h)$ , which we have used in our recent works,<sup>1,22,29,36</sup> includes competing long and short-range forces of the form<sup>12</sup>

$$\prod(h) = \kappa f(h) = \kappa \left[ \left( \frac{h_*}{h} \right)^n - \left( \frac{h_*}{h} \right)^m \right] \quad (2)$$

where  $\kappa$  is proportional to the Hamaker constant,  $h_*$  is the equilibrium film thickness, and the exponents satisfy  $n > m > 1$ . The first term represents liquid–solid repulsion, while the second term stands for the attractive force, and both terms cancel out for a flat film of thickness  $h_*$ . Within this model,

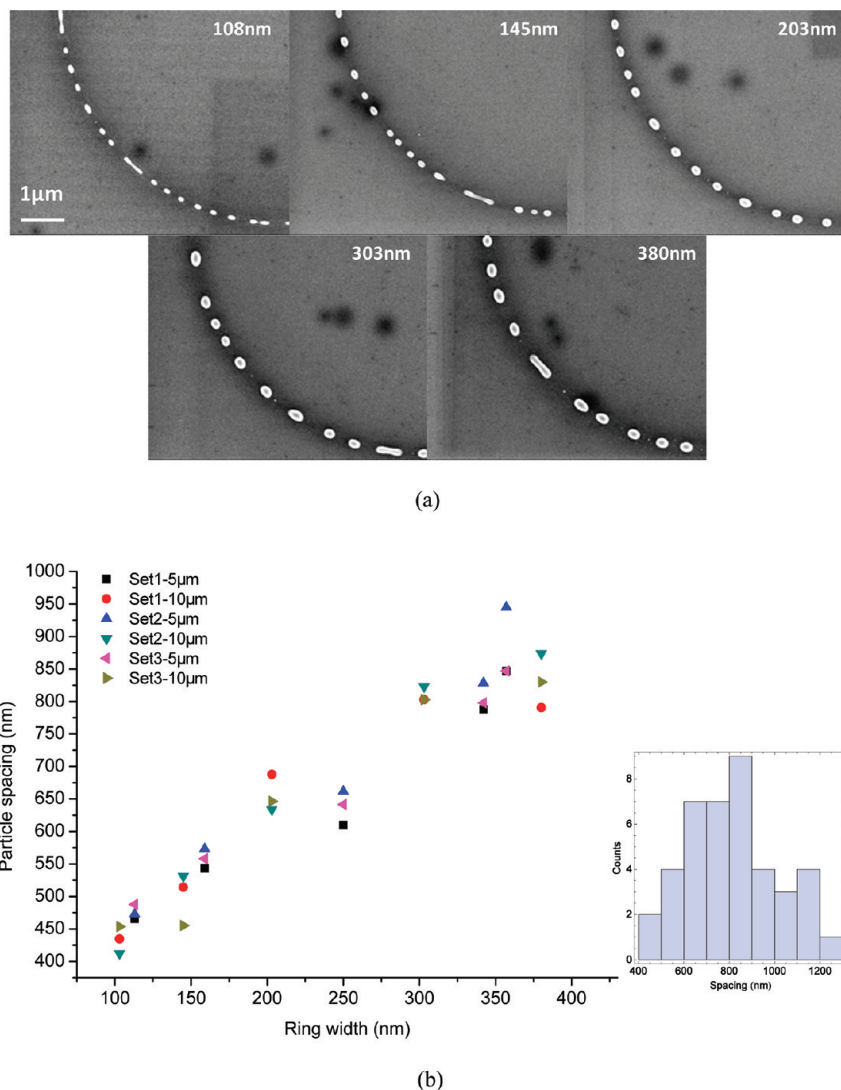


**Figure 3.** (a) Scanning electron micrographs of the  $h_0 = 15$  nm thick,  $r_1 = 5 \mu\text{m}$  radius copper rings of variable widths after five pulses. (b) Plot of average nanodrop spacing for fifteen  $5 \mu\text{m}$  and fifteen  $10 \mu\text{m}$  radius rings as a function of the measured widths. Inset shows the histogram of the droplet spacing (lower right) for 380 nm wide rings of  $5 \mu\text{m}$  radius.

$\kappa = S/(Mh_*)$ , where  $S$  is the spreading parameter and  $M = (n - m)/((m - 1)(n - 1))$ . The spreading parameter can be related to the apparent contact angle  $\theta$  via the Laplace–Young condition  $S = \gamma(1 - \cos \theta)$ . Use of the lubrication approximation for the problem characterized by large contact angle and related accuracy issues are discussed in previous works.<sup>1,29,36</sup>

The numerical procedure that is implemented to solve 2D eq 1 is based on the alternating direct implicit (ADI) type of simulations which are described in detail elsewhere.<sup>37</sup> The ADI approach to numerical computations turns out to be much more efficient than the fully implicit discretization used, for example, in ref 1. To ensure accuracy, we have run selected simulations using both methods and obtained identical results. These 2D simulations are carried out in a square computational domain of size  $L \times L$  divided into cells of size  $\Delta x \times \Delta y$  (typically, we use  $\Delta x = \Delta y = 5$  nm). We also carry out 1D simulations where we simulate only a cross section of a ring. These simulations are much less demanding computationally and are carried out in a domain of length  $L$  using the same fully implicit approach implemented

**Table 1. Cu Thin Film Properties at Melting Temperature**

$Y_{\text{Cu/Vacc}}$ (N/m)	$Y_{\text{SiO}_2/\text{Vacc}}$ (N/m)	$Y_{\text{Cu/SiO}_2}$ (N/m)	$\eta_{\text{Cu}}$ (Pa·S)	$\theta_{\text{Cu/SiO}_2}$ (measured)
1.304	0.31	0.34	$4.38 \times 10^{-3}$	79

previously.<sup>1</sup> We note that all the results that follow are fully converged, as verified by grid refinement.

In order to simulate the experimental configuration, the ring profile defined by using the following expression

$$h_{\text{ring}}(x, y, 0) = \frac{(h_0 - h^*)}{\pi} [\tan^{-1}(q(r - r_1)) - \tan^{-1}(q(r - r_2)) + h^*] \quad (3)$$

is perturbed as stated below. Here,  $r = (x^2 + y^2)^{1/2}$  and  $r_1$  and  $r_2$  are the internal and external radii of the ring, respectively. In order to have a relatively abrupt jump of  $h(x, y, 0)$  at  $r_1$  and  $r_2$ , we choose  $q = 100$ . We have verified that the main features of the

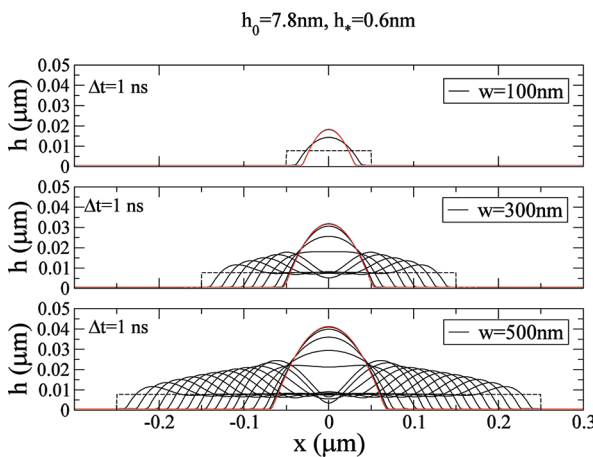


**Figure 4.** Temporal profiles from 1D time-dependent simulations of the  $h_0 = 7.8$  nm thick copper ring cross section for  $w = 100, 300$ , and  $500$  nm wide rings (ignoring azimuthal curvature), demonstrating the time scale for formation of a semicylindrical shape for each ring width.

results do not depend on the details of the initial condition. Note that  $h_0$  is the fluid thickness relative to the equilibrium film thickness,  $h_*$ . At the boundaries of the numerical domain, we impose no-flow boundary conditions; that is, the first and third derivatives of  $h(x,y,t)$  are zero along the sides of the square of linear dimension  $L$ . We use  $L = 1.1r_2$ .

In order to simulate the experimental noise, we perturb  $h_{\text{ring}}$  by a varicose mode which shifts the radial thickness profile depending on the azimuthal angle,  $\theta$

$$h_{\text{pert}}(r, \theta, 0) = \begin{cases} h_{\text{ring}}(r - \delta(\theta)) & r < r_0 \\ h_{\text{ring}}(r + \delta(\theta)) & r > r_0 \end{cases} \quad (4)$$

where  $r_0 = (r_1 + r_2)/2$  and the shift  $\delta(\theta)$  is given by a superposition of monochromatic modes with random amplitudes  $A_n$  ( $|A_n| < A_{\max}$ )

$$\delta(\theta) = \sum_{n=1}^N A_n \cos(n\theta) \quad (5)$$

We use  $N = 50$  and  $A_{\max} = 0.5$  nm.

#### 4. ESTIMATING THE HAMAKER CONSTANT

Finding the equilibrium thickness,  $h_*$ , is critical to determine the length and time scales associated with the ring instabilities. While the details of the morphology and length scale evolution of 2D thin films of copper on  $\text{SiO}_2$  will be discussed in a separate work, we here briefly summarize our results. Following our previous method (as well as the work of Kalyanaraman and co-workers<sup>16–19</sup>), we first find the Hamaker constant  $A$  and then find  $h_*$  using  $A = 6\pi\kappa h_*^3$  (ref 1) by finding a typical distance due to spinodal instabilities. Thin films of copper with four different thicknesses were sputter deposited onto 100 nm  $\text{SiO}_2$  coated silicon chips.<sup>38</sup> The copper film thicknesses were measured via optical reflectometry to be 4.8, 6.5, 7.5, and 8.5 nm, respectively. The samples were laser treated with 230 mJ/cm<sup>2</sup> pulses, sufficient for the film in each sample to dewet and form nanodroplets. The morphologies of different stages of dewetting were captured by scanning electron microscopy (SEM), and the characteristic length scale for each stage was evaluated by using fast Fourier transforms (FFTs) of the image, while resultant droplet sizes

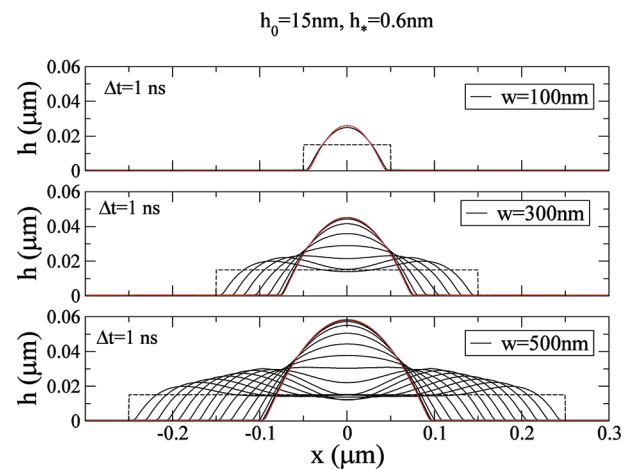


**Figure 5.** Temporal profiles from 1D time-dependent simulations of the  $h_0 = 15$  nm thick copper ring cross section for  $w = 100, 300$ , and  $500$  nm wide rings (ignoring azimuthal curvature).

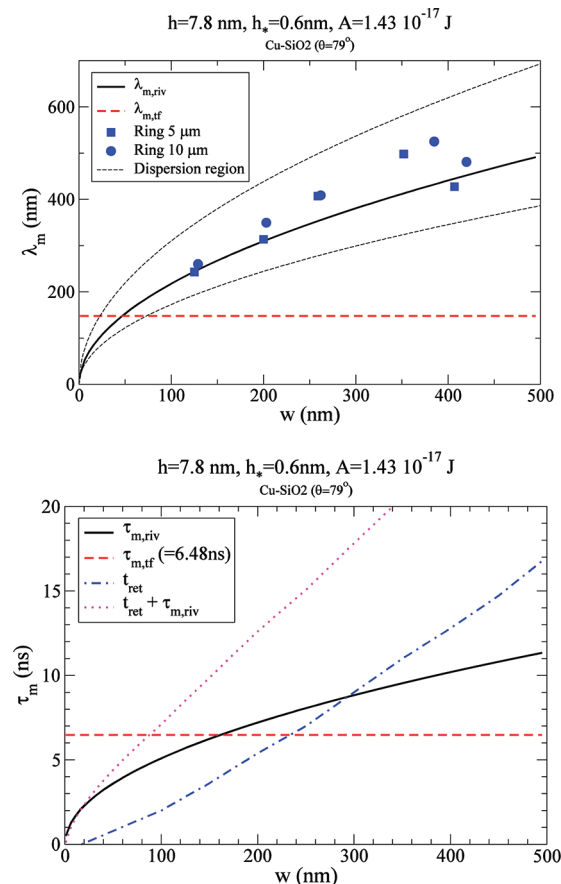


**Figure 6.** Length and time scales from LSA and simulations for the  $h_0 = 7.8$  nm thick copper ring as a function of the width,  $w$ . (Top) Wavelength of maximum growth rate,  $\lambda_m$  (nm), for the R-P (solid line,  $\lambda_{m,\text{riv}}$ ) and thin film (dashed line,  $\lambda_{m,\text{tf}}$ ) instabilities with experimental ring spacings (symbols) included, illustrating the comparison of length scale for a R-P instability and thin-film (spinodal) instability for various ring width. The dot-dashed lines limit a region of expected values of the spacing according to the standard deviations of the measured spacing between drops. (Bottom) Inverse of maximum growth rate,  $\tau_m$  =  $1/\lambda_m$  for the R-P ( $\tau_{m,\text{riv}}$ , solid line), thin film (spinodal) ( $\tau_{m,\text{tf}}$ , dashed line) instabilities and numerically calculated retraction times,  $t_{\text{ret}}$  obtained from Figure 4.

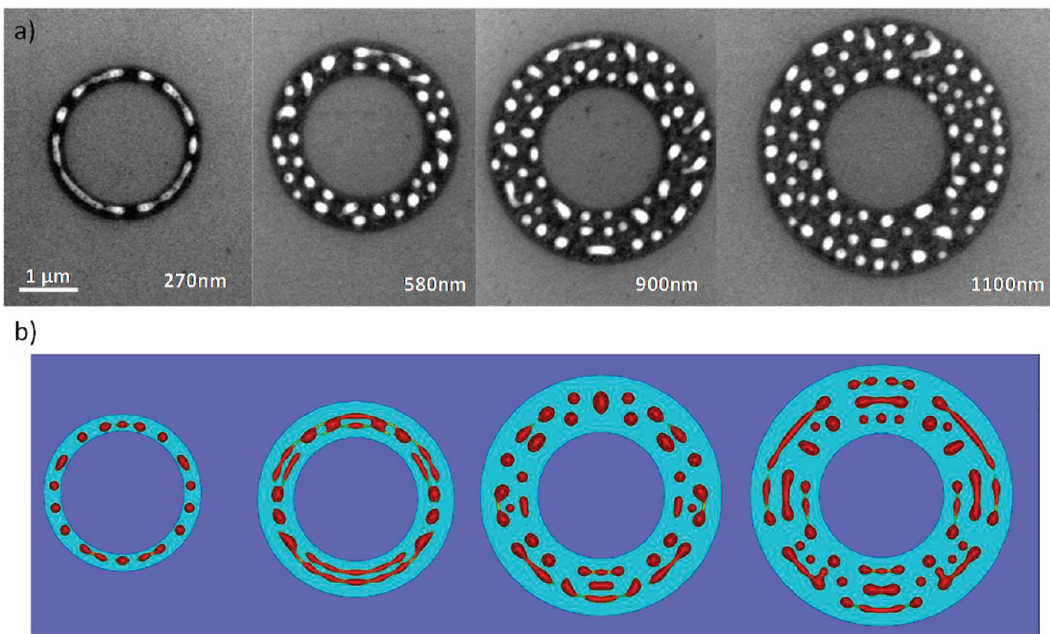


**Figure 7.** (a) Scanning electron micrographs of the  $h_0 = 7.8$  nm thick, 1  $\mu\text{m}$  radius copper rings of variable ring widths. Left-to-right:  $w = 270, 580, 900,$  and  $1100$  nm. (b) Snapshots of nonlinear 2D simulations of these rings in (a) at  $t = 100$  ns (light blue background shows the original ring).

were determined using an image analysis algorithm. As expected, for all the Cu thin films observed here, a characteristic length scale associated with spinodal dewetting is established at the very early stages of dewetting pattern evolution, which is indicated by both the SEM images and radial distribution functions of the FFTs. Different from our work of copper on silicon, we used the length scale associated with the initial hole formation to determine the equilibrium thickness scale for earliest times. The resultant Hamaker coefficient and equilibrium thickness for the hole formation associated with the thin film instability are found to be  $1.43 \times 10^{-17}$  J and  $h_* = 0.6$  nm, respectively.

## 5. ONE-DIMENSIONAL (1D) SIMULATIONS AND LINEAR STABILITY ANALYSIS

Once the Hamaker constant relevant for our system is known and using the film properties listed in Table 1, we proceed to consider the evolution of the strip geometry, using the model from section 3.

In this section, we neglect the in-plane radius of curvature of the ring. This approach has been discussed and justified elsewhere.<sup>1</sup> Thus, we consider just the cross section of a straight liquid copper strip on SiO<sub>2</sub> of width comparable to experiments. Time dependent simulations of the corresponding 1D version of eq 1 are performed to understand the evolution of the originally (approximately) rectangular cross section strip into a rivulet of almost cylindrical cross section. Figure 4 shows the evolution of the thickness profiles with  $h_0 = 7.8$  nm and widths  $w = 100, 300,$  and  $500$  nm. A 100 nm wide strip simply redistributes material to minimize the surface area according to contact line dynamics. On the other hand, the 300 and 500 nm wide strips contract until they reach the equilibrium semicylindrical shape. The time periods required to reach this final state, which we call retraction times, are  $t_{\text{ret}} \sim 10$  and  $18$  ns for the 300 and 500 nm wide strips, respectively. Figure 5 shows the cross sections of 15 nm thick film of widths  $w = 100, 300,$  and  $500$  nm. Again, the 100 nm wide strip

simply redistributes material to minimize the surface area, while the 300 and 500 nm wide strips contract until they reach the equilibrium shape. The retraction times are  $t_{\text{ret}} \sim 9$  and  $16$  ns for the 300 and 500 nm wide strips, respectively.

Following our previous work for liquid copper on silicon substrates, we first consider the results of linear stability analysis (LSA) of a thin film of thickness  $h_0$ , using the expression for the wavelength of maximum growth as<sup>36</sup>

$$\lambda_{\text{m,tf}} = 2\pi \left[ \frac{\kappa}{2\gamma} \left. \frac{df}{dh} \right|_{h_0} \right]^{-1/2} \quad (6)$$

and the corresponding growth rate as

$$\sigma_{\text{m,tf}} = \frac{16\gamma\pi^4}{3\mu} \frac{h_0^3}{\lambda_{\text{m,tf}}^4} \quad (7)$$

Even though this theory corresponds to flat films of infinite extension, we expect that this type of instability may develop on films characterized by length scale longer than  $\lambda_{\text{m,tf}}$  assuming that no other competing effect influences the evolution on the times scales comparable to  $\tau_{\text{m,tf}} = 1/\sigma_{\text{m,tf}}$ . Considering now stability of a rivulet of a given cross section  $A = h_0 w$  in equilibrium under capillary and van der Waals forces, we have<sup>22</sup>

$$\lambda_{\text{m,strip}} = 2\pi(2A)^{1/2} \left( \frac{M}{1 - \cos \theta} \right)^{1/4} \quad (8)$$

with the growth rate<sup>21,22</sup>

$$\sigma_{\text{m,strip}} = \frac{\gamma}{6\mu} F(\theta) A^{-1/2} \quad (9)$$

where

$$F(\theta) = 0.0379 \frac{\theta^3}{\sin \theta} \left( \theta - \frac{\sin 2\theta}{2} \right)^{1/2} \quad (10)$$

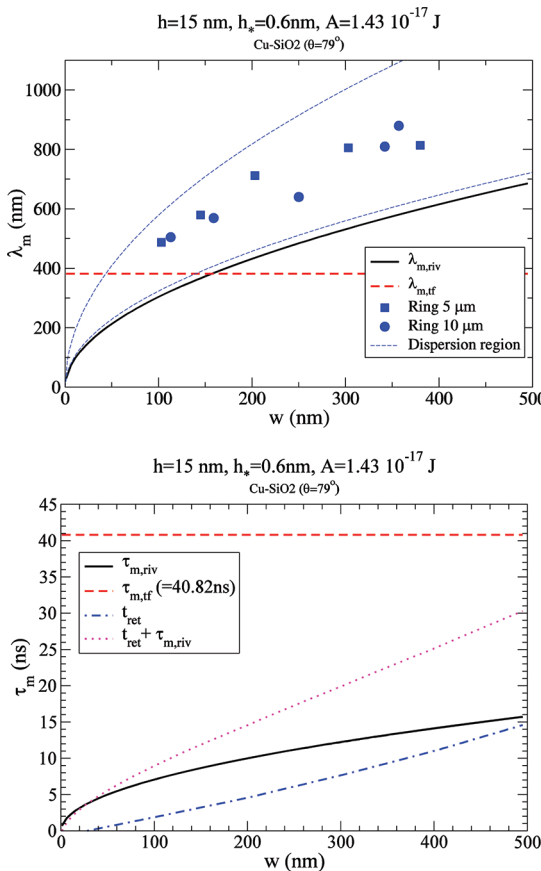


**Figure 8.** Length and time scales from LSA and simulations for the  $h_0 = 15$  nm thick copper strip as a function of the width,  $w$ . (Top) Wavelength of maximum growth rate,  $\lambda_m$ , for the R-P (solid line,  $\lambda_{m,\text{riv}}$ ) and thin film (dashed line,  $\lambda_{m,\text{tf}}$ ) instabilities with experimental ring spacings (symbols) included, illustrating the comparison of length scale for a R-P instability and thin-film (spinodal) instability for various ring width. The dot-dashed lines limit a region of expected values of the spacing according to the standard deviations of the measured spacing between drops. (b) Inverse of maximum growth rate,  $\tau_m = 1/\sigma_m$ , for the R-P - ( $\tau_{m,\text{riv}}$ , solid line), thin film (spinodal) ( $\tau_{m,\text{tf}}$  dashed line) instabilities, and numerically calculated retraction times,  $t_{\text{ret}}$ , obtained from Figure 5.

It should be pointed out that the wavelengths of maximum growth predict only approximately the expected distance between the drops, since the wavelengths close to  $\lambda_m$  have only slightly smaller growth rates; thus, a dispersion of growth rates exists and results in a dispersion in nanoparticle spacing as discussed above. This dispersion was discussed in detail in ref 32 where it was shown that additional “synthetic perturbation” can be used to produce uniformly spaced nanodrops/particles.

## 6. EXPERIMENTS WITH RINGS

In order to analyze the experimental results, we consider the basic processes involved in the evolution from the initial ring to final nanoparticles: the retraction of the contact lines of the original ring, and the eventual development of an instability of either thin-film or R-P type, or both. Each of the processes has its typical time scale, namely,  $t_{\text{ret}}$ ,  $\tau_{m,\text{tf}}$  and  $\tau_{m,\text{riv}} = 1/\sigma_{m,\text{riv}}$  respectively.

The influence of these three time scales on ring dewetting is analyzed in what follows for two different initial thicknesses,

$h_0$ , by comparison with both 1D and 2D simulations, using the Hamaker constant calculated above, and the material properties listed in Table 1 for  $(n,m) = (3,2)$ . We note that most of our conclusions will be based on further use of linear stability analysis, which only approximately describes nonlinear processes responsible for instability and breakup. Therefore, we are not looking for exact agreement, but rather to understand the main features of the experimental results.

**6.1. Thickness  $h_0 = 7.8$  nm.** Figure 6, top shows  $\lambda_{m,\text{tf}}$  (dashed line) and  $\lambda_{m,\text{riv}}$  (solid line) for  $h_0 = 7.8$  nm as given by eqs 3 and 5, as well as experimental data (symbols) extracted from Figure 2b. In Figure 2b, we showed the average drop spacing for individual rings measured using the length of the ring divided by the number of drops, while for clarity here each point represents the averaged spacing of three rings that each have the same ring width. As shown in Figure 6, top, this average distance between the droplets resulting from rings with  $w < \sim 350$  nm progressively increases and basically follows the length scale expected from R-P instability mechanism, although there is some overshoot for the widths of  $\sim 300$  nm. As already mentioned for  $w > 350$  nm, the data may be suggesting saturation or even a downward trend; however, in contrast with the Cu rings on Si substrate,<sup>1</sup> no clear transition to a constant spacing following thin-film instability mechanism is observed. In addition to the average spacing between the particles, Figure 6, top also shows the dispersion of the particle spacing, which is calculated as a standard deviation of the distance between drops. To simplify the figure, we show the dispersion using curves obtained by interpolating actual experimental results for different ring widths so that they appear as smooth dot-dashed lines. Clearly, dispersion is significant; this is expected based on the R-P model, since multiple wavelengths have comparable growth rates. Other sources of the dispersion will be discussed below in the context of 15 nm Cu rings.

We note that Trice et al. also observed a significant discontinuity in the spacing of cobalt and iron thin films on silicon oxide as a function of increasing film thickness and showed that the sign and magnitude of the thermal gradient can cause size and spacing length scale changes.<sup>18</sup> Similarly to the case of Cu on Si,<sup>1</sup> this mechanism does not appear to be operative in the liquid Cu–SiO<sub>2</sub> rings considered here since the film thicknesses for all the rings are the same and the simulated thermal gradient in the Cu on SiO<sub>2</sub> is less than  $\sim 0.07$  K/nm.

Figure 6, top shows the three time scales associated with  $h_0 = 7.8$  nm. For illustration, we will specifically examine the breakup process of three representative strip widths, 100 nm, 300 nm, and 500 nm, based on the calculated time scales.

First, for the 100 nm wide ring, we obtain that the time for the rivulet to reach its equilibrium shape is  $t_{\text{ret}} \sim 2$  ns which is less than the thin film instability time ( $\tau_{m,\text{tf}} = 6.5$  ns). Thus, the dynamics of the rivulet formation occur faster than the thin film instability, and the subsequent rivulet is expected to break up via a R-P instability in the circumferential direction with an additional time scale of  $\sim 5$  ns and length scale ( $\sim 218$  nm wavelength) associated with the new rivulet geometry (see dotted line in Figure 6, bottom), consistently with the experimental data shown in Figure 6, top.

For 300 and 500 nm rings, Figure 6, bottom shows that the time scale for thin-film instability is shorter than the retraction time. However, the difference is not very large, and furthermore we should also recall that  $\tau_{m,\text{tf}}$  is computed assuming infinite extension of a film. Therefore, it is not surprising that the R-P mechanism is still relevant in determining the distance between particles. The signature of the thin-film related instability

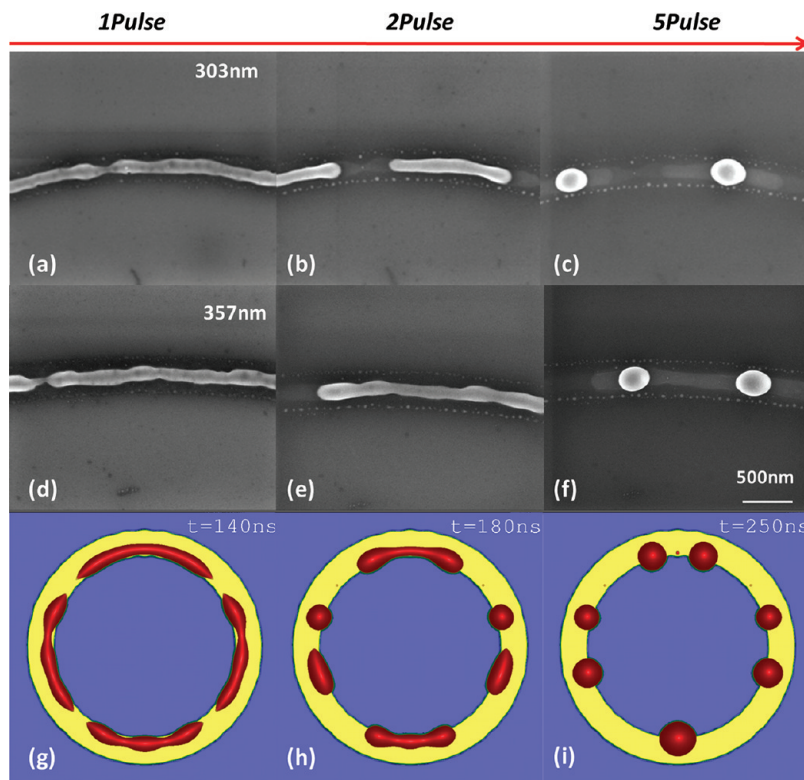


**Figure 9.** Scanning electron images of the 15 nm thick rings of the same ring regions ((a–c) 303 nm wide and (d–f) 357 nm wide) with progressively longer liquid lifetime (laser pulses) illustrating the circumferential transport which competes with the instability growth and leads to larger than predicted length scales. (g–i) 2D simulations of a 350 nm wide ring at different liquid lifetimes which illustrates that the fastest growing modes pinch off and subsequently coarsen the original instability length scale.

occurring during the retraction of the initial ring may be possibly seen in the experimental data for widths larger than  $\sim 350$  nm, although the trend is not strong enough to allow for making any precise conclusions, in particular considering large dispersion.

Another question is why we do not observe breakup in the radial direction, since the wavelength of maximum growth for thin-film instability may be smaller than the ring width. Figure 4 suggests in particular that  $w = 500$  nm should be close to radial breakup; however, the retraction is fast enough to prevent it from occurring. This is in contrast to similar Cu rings on Si, where the radial breakup does take place (see Figure 6 in ref 1). In the case considered here, we conjecture that larger contact angles lead to faster radial retraction that consequently prevents the breakup.

To further explore the degree to which the theoretical model can predict the experimental results, we synthesized a second set of rings with  $h_0 = 7.8$  nm for a broader range of ring widths, this time with  $w$  ranging from 270 to 1100 nm. To allow for direct comparison with simulations, these rings have small radii ( $r_1 = 1 \mu\text{m}$ ), so that 2D simulations can be carried out using reasonable computational resources. Figure 7a shows the results for  $w = 270, 580, 900$ , and  $1100$  nm exposed to two pulses of  $160 \text{ mJ/cm}^2$ . We see a clear transition from a single rivulet to multiple pseudoconcentric rings. Comparable 2D numerical simulations shown in Figure 7b indicate very similar evolution, where we can see perhaps more clearly that the original ring evolves into two rings in this particular case. These two rings subsequently break up following an R-P mechanism. Animations of the simulations results, available in the Supporting Information, clearly show this process.

**6.2. Thickness  $h_0 = 15$  nm.** Figure 8, top shows averaged experimental data from Figure 3b, together with the dispersion curves calculated in the same manner as for rings with  $h_0 = 7.8$  nm. In addition, we show the wavelengths of maximum growth expected from R-P and thin film mechanisms (solid line). Figure 8, bottom shows the three time scales associated with the breakup of these rings, namely,  $t_{\text{ret}}$ ,  $\tau_{m,\text{riv}}$ , and  $\tau_{m,\text{tf}} = \sim 41$  ns. We see that, for all these rings,  $t_{\text{ret}}$  combined with  $\tau_{m,\text{riv}}$  is significantly shorter than corresponding  $\tau_{m,\text{tf}}$  and hence all these thicker rings are predicted to break up via R-P instability. This prediction is in general agreement with the experimental trend in Figure 9a. However, the experimental average spacing is consistently longer than the wavelength of maximum growth resulting from the R-P mechanism. Experimental evidence from macroscopic rivulets with similar contact angles as those present here<sup>40</sup> is consistent with this trend. In these experiments, where the contact angles were large, wide and thick rivulets tend to produce larger drop spacing than that predicted by LSA. While a part of the answer to the difference in the calculated and observed difference may be related to the large dispersion of experimental results, or to the fact that LSA applied to a problem characterized by large contact angles provides only approximate results, one wonders if some additional mechanism is in place.

To explore this issue further, we consider the time evolution of the instability in both experiments and 2D simulations. Figure 9 shows combined experimental and computational results which can shed some light on the involved phenomena. In the experimental part (Figure 9a–f), we observe the instability evolution for  $w = 303$  and  $357$  nm and  $h_0 = 15$  nm. In the computational

part (Figure 9g–i), we show the results of 2D simulations carried out with  $h_0 = 15$  nm and  $w = 350$  nm for  $r_1 = 1 \mu\text{m}$  radius (small radius is again used for computational reasons). We show the profiles at  $t = 140, 180$ , and  $250$  ns with the original ring width shown on each (see the Supporting Information for a full movie of the 2D simulation). The distance between the drops in experiments (see Figure 9c and f) appears large compared to the wavelength of the undulations which can be seen in Figure 9a and d. One example of a similar effect in the simulations can be seen at the lower part of the ring where the relatively long rivulet in Figure 9h collapses to a single drop in part (i). We explain this effect as follows. The original ring initially breaks into parts at few locations (four in the example shown in Figure 9h), leading to rivulets which are longer than the wavelength of maximum growth rate. These rivulets, if sufficiently long, consequently break up into drops. However, if the rivulets are *not* sufficiently long (approximately twice as long as the wavelength of maximum growth for R-P instability), they may collapse just to a single drop. For clarity, we call this the “finite-size” effect. An additional contribution is contraction in the azimuthal direction due to capillary force and finite length of the rivulets, discussed in details in ref 22. Finite-size effect acts in one direction only, that is, leading to an increase of the spacing between the drops, as observed in the experimental results shown in Figure 9a, and it becomes particularly important when the number of drops is relatively small, as it is the case for wider rings. For more narrow rings, the wavelength of maximum growth is small and therefore the finite-size effect is not as significant, although some overshoot in the distance between the particles can be seen also for wider 7.8 nm thick rings (Figure 6, top).

Other possible causes not included in our theoretical model that can be taken into account to explain the shift of the average spacing are thermal diffusion or additional dissipation effects. One can expect that, as in the usual R-P instability, the small wavelengths are more affected by these effects leading to a significant reduction in their growth rates. As a consequence, the maximum growth rate is also reduced and its corresponding wavelength is shifted to larger values. Similar departures from the classical R-P predictions were also reported in previous experiments with molten bridges<sup>41</sup> produced by ring heaters in the absence of gravity where the effect of thermal gradient can lead to anomalously long stable bridges.

Finally, one may wonder why a similar overshoot of the distance between the drops was not observed for the Cu on Si rings discussed in ref 1. In that configuration, it was found that R-P prediction is consistent with the results in the regime where R-P mechanism is the relevant one. The difference between the two cases is that for Cu on Si there is stronger influence of thin-film instability, leading to a different (constant) scaling of the distance between the drops as ring widths are increased beyond  $\sim 200$  nm for a comparable 13 nm thick Cu strip (see Figure 4a in ref 1). Furthermore, the large contact angle in the present work leads to a speed-up of the azimuthal contraction, therefore reducing the probability of consequent breakups. These effects will be explored in future work using nickel on  $\text{SiO}_2$  which has a larger spreading parameter, and preliminary results suggest a more dramatic effect.

## 7. CONCLUSIONS

The instabilities of nanopatterned copper rings on  $\text{SiO}_2$  have been studied. Thin rings (7.8 nm) are found to contract to form liquid rings which subsequently break up into drops/particles via

the mechanism resembling Rayleigh–Plateau (R-P) instability. In contrast to the experiments carried out on Si, reported in ref 1, we do not find a clear signature of the decrease of the distance between the particles as the ring widths are increased, although some signs of saturation of this distance as a function of ring width are observed. This difference between the experiments on Si and  $\text{SiO}_2$  is qualitatively explained by considering the time scales that govern the instability process; for the rings on  $\text{SiO}_2$ , we find that the dominance of thin-film instability is not as strong as in the case of Si surface, consistent with the experimental results. Thicker rings (15 nm) show continuous increase of the distance between the particles as ring widths are increased, consistent with the R-P mechanism.

For both thin and thick rings, we find that the distance between the particles is larger than the one predicted by the R-P mechanism modified by the presence of the solid substrate. This difference between experimental results and the prediction of the R-P model is particularly significant for thicker rings. We discuss possible reasons for this difference, ranging from nonlinear effects combined with the fast circumferential transport, the use of lubrication approximation in the problem where contact angles are relatively large, to quenching of the instability for short wavelengts by effects not considered in the theoretical model. While clearly future work is needed to understand the details of the breakup of metal rings on the nanoscale, we find that a significant insight can be reached by using a relatively simple hydrodynamic model combined with accurate numerical simulations. Ultimately, we envisage that a thorough understanding of the relevant and competing instability time and length scales will enable the design of ordered nanoparticle arrays with specific size and spacing and thus functionality.

## ■ ASSOCIATED CONTENT

**S Supporting Information.** Animations of the break up of rings from the results of 2D numerical simulations for 270, 580, 900, and 1100 nm wide rings exposed to two laser pulses of  $160 \text{ mJ/cm}^2$ . Animations of the result of 2D simulation for 15 nm thick ring with  $w = 350$  nm and  $r_1 = 1 \mu\text{m}$ . This material is available free of charge via the Internet at <http://pubs.acs.org>.

## ■ ACKNOWLEDGMENT

P.D.R., J.D.F., and Y.W. acknowledge support from the U.S. Department of Energy, Basic Energy Sciences, Materials Sciences and Engineering Division for sponsoring the aspects of this work related to understanding the fundamental mechanisms operative during liquid phase, thin film dewetting. L.K., P.D.R., and J.D.F. also acknowledge that the lithography and electron imaging results reported in this Article were conducted at the Center for Nanophase Materials Sciences, which is sponsored at Oak Ridge National Laboratory by the Office of Basic Energy Sciences, U.S. Department of Energy. L.K. acknowledges support by the NSF Grant No. DMS-0908158. J.A.D. and A.G.G. acknowledge CONICET-Argentina for travel support within the International Cooperation Program, and ANPCyT-Argentina for support within the project PICT 2498/06.

## ■ REFERENCES

- (1) Wu, Y. Y.; Fowlkes, J. D.; Rack, P. D.; Diez, J. A.; Kondic, L. *Langmuir* **2010**, *26*, 11972.

- (2) Bonnemann, H.; Endruschat, U.; Tesche, B.; Rufinska, A.; Lehmann, C. W.; Wagner, F. E.; Filoti, G.; Parvulescu, V.; Parvulescu, V. I. *Eur. J. Inorg. Chem.* **2000**, *5*, 819.
- (3) Guan, Y. F.; Melechko, A. V.; Pedraza, A. J.; Simpson, M. L.; Rack, P. D. *Nanotechnology* **2007**, *18*, 335306.
- (4) Bonnemann, H.; Waldfchner, N.; Haubold, H. G.; Vad, T. *Chem. Mater.* **2002**, *14*, 1115.
- (5) Ghodselahti, T.; Vesaghi, M. A.; Shafiekhan, A. *J. Phys. D: Appl. Phys.* **2009**, *42*, 015308.
- (6) Lin, C. H.; Jiang, L.; Zhou, J.; Xiao, H.; Chen, S. J.; Tsai, H. L. *Opt. Lett.* **2010**, *35*, 941.
- (7) Picciotto, A.; Pucker, G.; Torrisi, L.; Bellutti, P.; Caridi, F.; Bagolini, A. *Radiat. Eff. Defects Solids* **2008**, *163*, 513.
- (8) Amekura, H.; Takeda, Y.; Kishimoto, N. *Nucl. Instrum. Methods Phys. Res., Sect. B* **2005**, *234*, 573.
- (9) Chan, G. H.; Zhao, J.; Hicks, E. M.; Schatz, G. C.; Van Duyne, R. P. *Nano Lett.* **2007**, *7*, 1947.
- (10) Beck, F. J.; Polman, A.; Catchpole, K. R. *J. Appl. Phys.* **2009**, *105*.
- (11) Wu, Y. Y.; Fowlkes, J. D.; Rack, P. D. *J. Mater. Res.* **2011**, *26*, 277.
- (12) Seemann, R.; Herminghaus, S.; Jacobs, K. *Phys. Rev. Lett.* **2001**, *86*, 5534.
- (13) Herminghaus, S.; Jacobs, K.; Mecke, K.; Bischof, J.; Fery, A.; Ibn-Elhaj, M.; Schlagowski, S. *Science* **1998**, *282*, 916.
- (14) Seemann, R.; Herminghaus, S.; Jacobs, K. *J. Phys.: Condens. Matter* **2001**, *13*, 4925.
- (15) Bischof, J.; Scherer, D.; Herminghaus, S.; Leiderer, P. *Phys. Rev. Lett.* **1996**, *77*, 1536.
- (16) Krishna, H.; Gangopadhyay, A. K.; Strader, J.; Kalyanaraman, R. *J. Magn. Magn. Mater.* **2011**, *323*, 356.
- (17) Krishna, H.; Sachan, R.; Strader, J.; Favazza, C.; Khenner, M.; Kalyanaraman, R. *Nanotechnology* **2010**, *21*, 155601.
- (18) Trice, J.; Favazza, C.; Thomas, D.; Garcia, H.; Kalyanaraman, R.; Sureshkumar, R. *Phys. Rev. Lett.* **2008**, *101*, 017802.
- (19) Trice, J.; Thomas, D.; Favazza, C.; Sureshkumar, R.; Kalyanaraman, R. *Phys. Rev. B* **2007**, *75*, 235439.
- (20) Becker, J.; Grun, G.; Seemann, R.; Mantz, H.; Jacobs, K.; Mecke, K. R.; Blossey, R. *Nat. Mater.* **2003**, *2*, 59.
- (21) Brochard-Wyart, F.; Redon, C. *Langmuir* **1992**, *8*, 2324.
- (22) Diez, J. A.; Gonzalez, A. G.; Kondic, L. *Phys. Fluids* **2009**, *21*, 082105.
- (23) Stone, H. A.; Stroock, A. D.; Ajdari, A. *Annu. Rev. Fluid Mech.* **2004**, *36*, 381.
- (24) Stone, H. A.; Kim, S. *AIChE J.* **2001**, *47*, 1250.
- (25) Ruschak, K. J. *Annu. Rev. Fluid Mech.* **1985**, *17*, 65.
- (26) Young, G. W.; Davis, S. H. *J. Fluid Mech.* **1987**, *176*, 1.
- (27) Sekimoto, K.; Oguma, R.; Kawasaki, K. *Ann. Phys.* **1987**, *176*, 359.
- (28) Langbein, D. *J. Fluid Mech.* **1990**, *213*, 251.
- (29) Kondic, L.; Diez, J. A.; Rack, P. D.; Guan, Y. F.; Fowlkes, J. D. *Phys. Rev. E* **2009**, *79*, 026302.
- (30) Rack, P. D.; Guan, Y.; Fowlkes, J. D.; Melechko, A. V.; Simpson, M. L. *Appl. Phys. Lett.* **2008**, *92*, 223108.
- (31) Fowlkes, J. D.; Wu, Y. Y.; Rack, P. D. *ACS Appl. Mater. Interfaces* **2010**, *2*, 2153.
- (32) Fowlkes, J. D.; Kondic, L.; Diez, J.; Wu, Y. Y.; Rack, P. D. *Nano Lett.* **2011**, *11*, 2478.
- (33) Bao, C.; Li, G. P.; Chen, X. M.; ChO, S. J.; Kim, H. *Chin. Phys. Lett.* **2008**, *25*, 1400.
- (34) Callegari, G.; Calvo, A.; Huhn, J. P.; Brochard-Wyart, F. *Langmuir* **2002**, *18*, 4795.
- (35) McCallum, M. S.; Voorhees, P. W.; Miksis, M. J.; Davis, S. H.; Wong, H. *J. Appl. Phys.* **1996**, *79*, 7604.
- (36) Diez, J. A.; Kondic, L. *Phys. Fluids* **2007**, *19*, 072107.
- (37) Lin, T.-S.; Kondic, L.; Filippov, A. arxiv.org preprint no. 1109.6353.
- (38) Klein, K. L.; Melechko, A. V.; Rack, P. D.; Fowlkes, J. D.; Meyer, H. M.; Simpson, M. L. *Carbon* **2005**, *43*, 1857.
- (39) Favazza, C.; Kalyanaraman, R.; Sureshkumar, R. *Nanotechnology* **2006**, *17*, 4229.
- (40) González, A. G.; Diez, J.; Gratton, R.; Gomba, J. *Europhys. Lett.* **2007**, *77*, 44001.
- (41) Chen, Y. J.; Abbaschian, R.; Steen, P. H. *J. Fluid. Mech.* **2003**, *485*, 97.